Spectral-element simulations of global seismic wave propagation—II. Three-dimensional models, oceans, rotation and self-gravitation

Dimitri Komatitsch and Jeroen Tromp

Seismological Laboratory, California Institute of Technology, Pasadena, CA 91125, USA. E-mail: jtromp@gps.caltech.edu

SUMMARY

We simulate global seismic wave propagation based upon a spectral-element method. We include the full complexity of 3-D Earth models, i.e. lateral variations in compressional-wave velocity, shear-wave velocity and density, a 3-D crustal model, ellipticity, as well as topography and bathymetry. We also include the effects of the oceans, rotation and self-gravitation in the context of the Cowling approximation. For the oceans we introduce a formulation based upon an equivalent load in which the oceans do not need to be meshed explicitly. Some of these effects, which are often considered negligible in global seismology, can in fact play a significant role for certain source–receiver configurations. Anisotropy and attenuation, which were introduced and validated in a previous paper, are also incorporated in this study. The complex phenomena that are taken into account are introduced in such a way that we preserve the main advantages of the spectral-element method, which are an exactly diagonal mass matrix and very high computational efficiency on parallel computers. For self-gravitation and the oceans we benchmark spectral-element synthetic seismograms against normal-mode synthetics for the spherically symmetric reference model PREM. The two methods are in excellent agreement for all body- and surface-wave arrivals with periods greater than about 20 s in the case of self-gravitation and 25 s in the case of the oceans. At long periods the effect of gravity on multiorbit surface waves up to R_4 is correctly reproduced. We subsequently present results of simulations for two real earthquakes in fully 3-D Earth models for which the fit to the data is significantly improved compared with classical normal-mode calculations based upon PREM. For example, we show that for trans-Pacific paths the Rayleigh wave can arrive more than a minute earlier than in PREM, and that the Love wave is much shorter in duration.

Key words: body waves, electrodynamics, global seismology, numerical techniques, seismic wave propagation, surface waves, tomography.

1 INTRODUCTION

In a previous paper (Komatitsch & Tromp 2002, hereafter referred to as Paper I) we demonstrated that the spectral-element method (SEM) can accurately simulate seismic wave propagation in spherically symmetric Earth models at periods greater than about 20 s. In this paper we introduce the full complexity of the 3-D Earth, i.e. lateral variations in compressional-wave velocity, shear-wave velocity and density in the mantle, a 3-D crustal model, as well as ellipticity, surface topography and bathymetry. We also introduce more complexity in the wave equation itself by talking into account the effects of the oceans, rotation and self-gravitation. The effects of the ocean are incorporated based upon an equivalent surface load without having to actually mesh the water layer. Self-gravitation, in the context of the Cowling approximation, is introduced in the SEM in a fashion similar to the innovative work of Chaljub (2000) and Chaljub *et al.* (2002). We validate the implementation of self-gravitation and the oceans

by comparison with normal-mode synthetics for the Preliminary Reference Earth Model (PREM) (Dziewonski & Anderson 1981).

In this paper we will be referring to equations and figures in Paper I using the notation (I.x), as in Fig. I.1 for Fig. 1 of Paper I.

2 MESHING THE 3-D EARTH

We use the mesh for a spherically symmetric Earth model developed in Paper I (Fig. I.6) as a starting point for a mesh for the 3-D Earth. Such a mesh is based on the concept of the 'quasi-uniform gnomonic projection', also known as the 'cubed sphere' (Sadourny 1972; Ronchi *et al.* 1996; Taylor *et al.* 1997), i.e. an analytical mapping between the six sides of a cube and the surface of the sphere (see Paper I for details, in particular Figs. I.1–6). The idea was introduced for global wave propagation by Taylor *et al.* (1997) and Chaljub (2000), and later used by Capdeville *et al.* (2002). Any reasonably smooth laterally heterogeneous shear-velocity, compressional-velocity or density model may be used in the mantle. In this paper
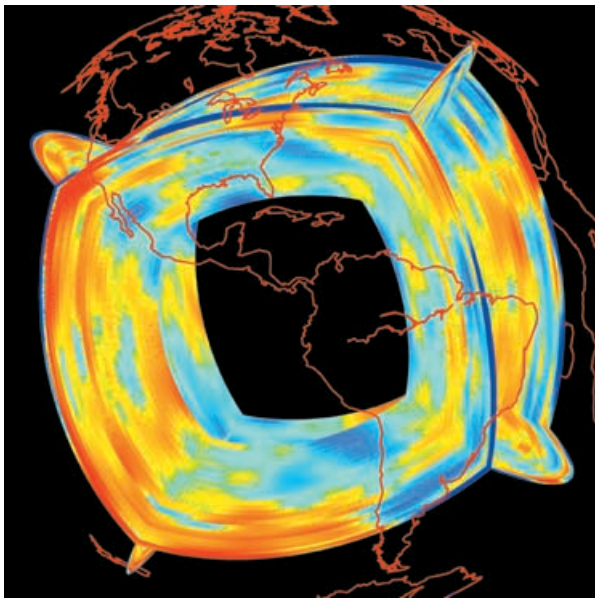
Figure 1. Mantle model S20RTS (Ritsema *et al.* 1999) is superimposed on the mesh. A 3-D density model is obtained by scaling the shear-wave velocity variations by a factor of 0.4, in accordance with mineral physics estimates. The figure shows lateral variations in shear velocity projected on to the four sides of the six chunks that constitute the cubed sphere mesh (see Figs I.1–6 for details). Blue colours denote faster than average shear-wave velocities and red colours denote slower than average shear-wave velocities.

we will use model S20RTS of Ritsema *et al.* (1999) (Fig. 1). Lateral variations determined by this model are superimposed on PREM (Dziewonski & Anderson 1981). Variations in density are obtained by scaling the shear-wave velocity variations by a factor of 0.4, in accordance with mineral physics estimates.

Every phase observed in a seismogram is affected by the Earth's crust, so it is important to incorporate a detailed crustal model in the mesh. We use Crust 2.0 (Bassin *et al.* 2000), which is a global $2° \times 2°$ crustal model (Fig. 2). This model is a significantly improved version of the $5° \times 5°$ model Crust 5.1 (Mooney *et al.* 1998). We do not incorporate the ice layer that is present in some regions of Crust 2.0, but we do include the sedimentary layers. The Moho depth in Crust 2.0 varies between 6.65 km (oceanic crust) and 75 km (underneath the Himalaya). The compressional-wave velocity at the surface of Crust 2.0, excluding the sedimentary layers, varies between 5.0 and 6.2 km s^{-1}, the shear-wave velocity varies between 2.5 and 3.2 km s^{-1}, and density varies between 2600 and 2800 kg m^{-3}. For comparison, PREM has an upper-crustal P velocity of 5.8 km s^{-1}, an S velocity of 3.2 km s^{-1} and a density of 2600 kg m^{-3}. We do not honour the shape of the Moho in the mesh, since it is too shallow in many locations (e.g. the oceanic crust) to squeeze spectral elements between the Moho and the surface without creating stability problems in the time-integration scheme. Instead, we assign Crust 2.0 velocities and density to the pre-existing mesh. We smooth Crust 2.0 to suppress its sharp transitions between $2° \times 2°$ blocks. The grid spacing along the surface is roughly 10 km, as in Paper I (4×240 spectral elements along a great circle, with five grid points in each lateral direction of an element).

Once the mantle and crustal models have been added, we make the Earth elliptical in shape (Fig. 3). The ellipticity as a function of depth is determined by solving Clairaut's equation (Dahlen & Tromp 1998), and the mesh is stretched or squashed accordingly.

(a)

(b)
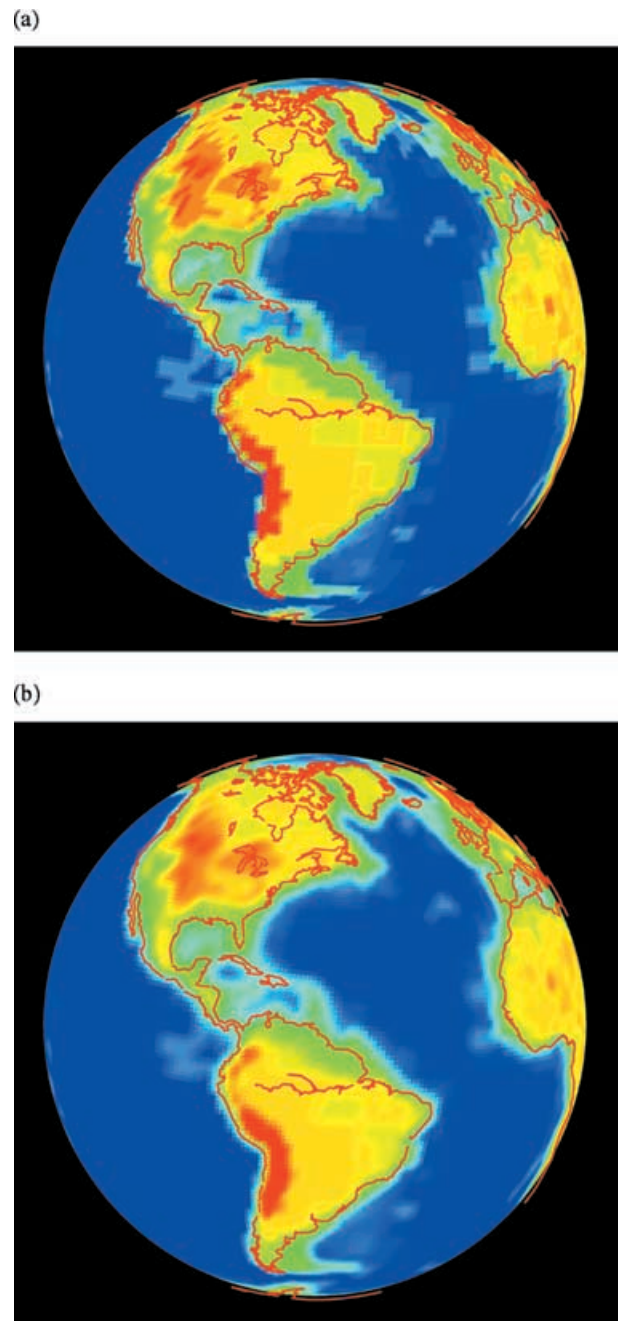
Figure 2. The $2° \times 2°$ crustal model Crust 2.0 (Bassin *et al.* 2000) is superimposed on the mesh. Because the model consists of blocks with constant properties (top), we smooth it by averaging over spherical caps with a $2°$ radius (bottom). The figure shows Moho depth (which varies between 6.65 and 75 km in the model). Red represents thicker than average crust and blue thinner than average crust.

Free-surface topography and bathymetry are also incorporated in the mesh (Fig. 4). We use the global 5×5 min^2 ETOPO5 bathymetry and topography model (NOAA 1988). The bathymetry map is also used to define the thickness of the oceans at the surface of the mesh in order to take into account the effects of the oceans on global wave propagation. As will be explained in Sections 3 and 4, the oceans are incorporated in the SEM by introducing an equivalent load at the ocean floor, without having to explicitly mesh the water layer.
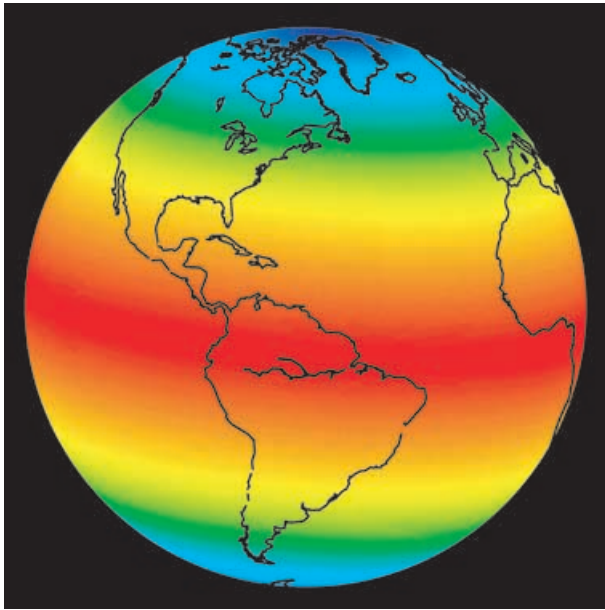
Figure 3. The ellipticity of the Earth is incorporated in the mesh. As a result of its rotation, the Earth is slightly flattened at the poles (blue colours) and elongated at the equator (red colours). The ellipticity at the surface is small ($\epsilon \simeq 1/300$).

Figure 5. Map of the thickness of the oceans and large lakes at the surface of the mesh. In Section 3 we use this map to represent the effects of the oceans on global wave propagation based upon an equivalent load, without having to explicitly mesh the oceans. The oceans represent about 75 per cent of the surface of the Earth (the colour scale indicates ocean depth) and the continents (yellow) about 25 per cent. The bathymetry map is taken from model ETOPO5 (NOAA 1988).

At this stage we therefore simply store a map of the thickness of the oceans (Fig. 5).

It is important to mention that, as in Paper I, the stability of the time-integration scheme, i.e. the value of the time step Δt, remains controlled by the size of the mesh near the inner-core boundary. The stability condition is therefore not affected by the introduction of 3-D heterogeneity.

3 THE SPECTRAL-ELEMENT METHOD

In this paper we incorporate the oceans, which are mostly relevant for free-surface reflected phases, such as *PP*, *SS* and *SP*, and for the dispersion of Rayleigh waves. We also include the effects of

(a)

(b)
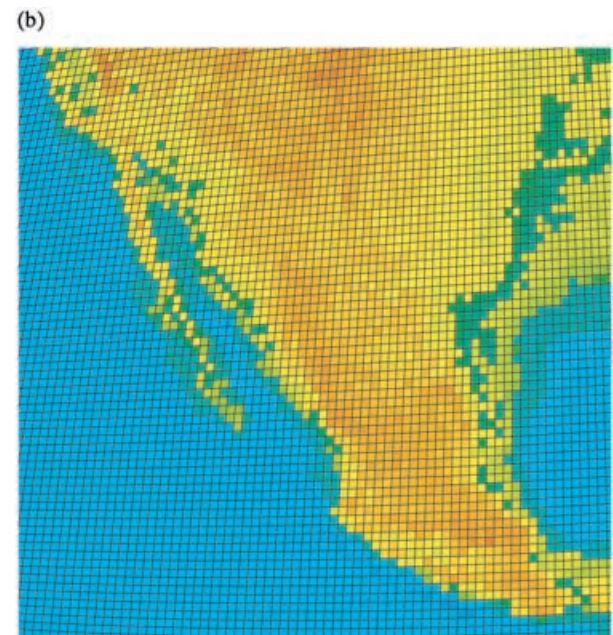
Figure 4. Topography and bathymetry of the Earth, obtained from the ETOPO5 model (NOAA 1988), is added to the mesh. Left: surface elements of the actual mesh used in this paper. The colour scale represents elevation with respect to the reference ellipsoid. One can see how accurately the mesh honours topography. Right: close-up of Mexico and the Southern United States showing the spectral elements in the mesh at the surface (grey squares). In each spectral element we use a polynomial degree $N = 4$ (see Paper I for details), therefore each surface mesh element contains $(N + 1)^2 = 25$ grid points, which translates into an average grid spacing of approximately 10 km at the surface.

self-gravitation, based upon the Cowling approximation need, and rotation, which are mostly relevant in the context of long-period surface waves.

3.1 Hydrostatic equilibrium

Throughout this paper we assume that the Earth is in hydrostatic equilibrium before the occurrence of an earthquake. For a rotating, self-gravitating Earth model this means that pressure gradients are balanced by gradients of the geopotential (e.g. Dahlen & Tromp 1998). Let P denote the initial pressure in the Earth model, let Φ denote the gravitational potential associated with the initial distribution of density ρ, and let ψ denote the centrifugal potential, which is defined in terms of the Earth's angular rotation vector $\boldsymbol{\Omega}$ by $\psi = -\frac{1}{2}[\Omega^2 r^2 - (\boldsymbol{\Omega} \cdot \mathbf{r})^2]$. Here $\mathbf{r}$ is the position vector, $r = |\mathbf{r}|$ denotes the radius and $\Omega = |\boldsymbol{\Omega}|$ is the angular rotation rate. In what follows, we will ignore the non-hydrostatic pre-stress, in which case hydrostatic equilibrium is determined by $\nabla P = -\rho \nabla (\Phi + \psi)$. This equation implies that equal surfaces of initial pressure P, density ρ and geopotential $\Phi + \psi$ coincide. As a result, these level surfaces are axially symmetric ellipsoids. Because we assume that we can neglect the non-hydrostatic pre-stress, there is no contradiction between this assumption and the fact that we use a 3-D density model in the mesh.

Suppose we start with a spherically symmetric, non-rotating Earth model. The gravitational potential Φ_0 of such an Earth model is determined by Poisson's equation: $\Phi_0'' + 2r^{-1}\Phi_0' = 4\pi G \rho_0$, where ρ_0 denotes the radial profile of density, G denotes the gravitational constant and a prime denotes differentiation with respect to radius r. If we define the magnitude of the gravitational acceleration to be $g_0 = \Phi_0'$, then we have

$$g_0' + 2r^{-1}g_0 = 4\pi G \rho_0. \tag{1}$$

The gravitational potential Φ in a slowly rotating, ellipsoidal Earth model is given by $\Phi = \Phi_0 + \frac{2}{3}(r\epsilon g_0 - \frac{1}{2}\Omega^2 r^2)P_2(\cos\theta)$ and the centrifugal potential ψ may be written in the form $\psi = -\frac{1}{3}\Omega^2 r^2 [1 - P_2(\cos\theta)]$, where ϵ denotes the ellipticity as a function of radius, P_2 is the degree-two Legendre function and θ denotes colatitude. The associated gravitational acceleration $\mathbf{g}$ is defined in terms of the gradient of the geopotential by

$$\mathbf{g} = -\nabla(\Phi + \psi)$$
$$= -\left[g_0 + \frac{2}{3}(\epsilon g_0 + r\epsilon' g_0 + r\epsilon g_0')P_2 - \frac{2}{3}\Omega^2 r\right]\hat{\mathbf{r}} - \frac{2}{3}\epsilon g_0 \partial_\theta P_2 \hat{\boldsymbol{\theta}}. \tag{2}$$

Here g_0' is determined by eq. (1) and the radial derivative of ellipticity ϵ' is usually defined in terms of the auxiliary function $\eta = r\epsilon'/\epsilon$ (Dahlen & Tromp 1998).

In the weak formulation of the equations of motion in the mantle and inner core we shall need the gradient of the gravitational acceleration, $\mathbf{H} = \nabla \mathbf{g}$, which is given by

$$\mathbf{H} = -\left[g_0' + \frac{2}{3}(2\epsilon' g_0 + 2\epsilon g_0' + 2r\epsilon' g_0' + r\epsilon'' g_0 + r\epsilon g_0'')P_2\right.$$
$$\left. - \frac{2}{3}\Omega^2\right]\hat{\mathbf{r}}\hat{\mathbf{r}} - \frac{2}{3}(\epsilon' g_0 + \epsilon g_0')\partial_\theta P_2(\hat{\boldsymbol{\theta}}\hat{\mathbf{r}} + \hat{\mathbf{r}}\hat{\boldsymbol{\theta}}) - r^{-1}\left[g_0\right.$$
$$+ \frac{2}{3}(\epsilon g_0 + r\epsilon' g_0 + r\epsilon g_0')P_2 - \frac{2}{3}\Omega^2 r + \frac{2}{3}r^{-1}\epsilon g_0 \partial_\theta^2 P_2\right]\hat{\boldsymbol{\theta}}\hat{\boldsymbol{\theta}}$$
$$- r^{-1}\left[g_0 + \frac{2}{3}(\epsilon g_0 + r\epsilon' g_0 + r\epsilon g_0')P_2 - \frac{2}{3}\Omega^2 r\right.$$
$$\left. + \frac{2}{3}r^{-1}\epsilon g_0 \cot\theta \partial_\theta P_2\right]\hat{\boldsymbol{\phi}}\hat{\boldsymbol{\phi}}. \tag{3}$$

The second derivative of ellipticity with respect to radius is determined by Clairaut's equation and the second derivative of the gravitational acceleration g_0'' may be obtained by differentiating eq. (1).

In most cases, however, we can neglect the contribution of ellipticity and rotation, since ϵ is very small ($\epsilon \simeq 1/300$ at the surface) and so is the Earth's rotation rate squared. Under these assumptions, eqs (2) and (3) reduce to

$$\mathbf{g} = -g_0\hat{\mathbf{r}} \tag{4}$$

and

$$\mathbf{H} = -g_0'\hat{\mathbf{r}}\hat{\mathbf{r}} - r^{-1}g_0(\hat{\boldsymbol{\theta}}\hat{\boldsymbol{\theta}} + \hat{\boldsymbol{\phi}}\hat{\boldsymbol{\phi}}), \tag{5}$$

respectively. These are the expressions that we will use in the rest of the paper.

3.2 Mantle and crust

In a rotating, self-gravitating Earth model, the elastic wave equation for the mantle and crust may be written in the form (Dahlen & Tromp 1998)

$$\rho\left(\partial_t^2 \mathbf{s} + 2\boldsymbol{\Omega} \times \partial_t \mathbf{s}\right) = \nabla \cdot \mathbf{T} + \nabla(\rho \mathbf{s} \cdot \mathbf{g}) - \rho\nabla\phi - \nabla \cdot (\rho\mathbf{s})\mathbf{g} + \mathbf{f}. \tag{6}$$

Here $\mathbf{T}$ denotes the stress tensor, which is related linearly to the displacement gradient $\nabla\mathbf{s}$ by Hooke's law (eq. I.6 in Paper I) in an elastic model, or by the generalization (I.9) in an anelastic model. The earthquake source is represented by the point force $\mathbf{f}$, which is given in terms of the moment tensor $\mathbf{M}$ by (I.14). The perturbed gravitational potential ϕ is determined by Poisson's equation within the Earth, $\nabla^2 \phi = -4\pi G \nabla \cdot (\rho\mathbf{s})$ and by Laplace's equation in the rest of space, $\nabla^2 \phi = 0$.

Because Laplace's equation is defined in all of space, solving the momentum eq. (6) in conjunction with Poisson's and Laplace's equations is rather daunting from a numerical perspective. The approach can be simplified considerably by making what is known as Cowling's approximation (Cowling 1941), as discussed by Valette (1987); Dahlen & Tromp (1998) and Chaljub (2000). In this approximation one ignores perturbations ϕ in the gravitational potential while retaining the unperturbed gravitational potential. Physically, this means that we ignore the effects of mass redistribution. Under this assumption the momentum equation (6) becomes

$$\rho\left(\partial_t^2 \mathbf{s} + 2\boldsymbol{\Omega} \times \partial_t \mathbf{s}\right) = \nabla \cdot \mathbf{T} + \nabla(\rho \mathbf{s} \cdot \mathbf{g}) - \nabla \cdot (\rho\mathbf{s})\mathbf{g} + \mathbf{f}. \tag{7}$$

The associated boundary conditions are that on the free surface the traction $\hat{\mathbf{n}} \cdot \mathbf{T}$, where $\hat{\mathbf{n}}$ denotes the unit outward normal to the free surface, needs to vanish. On the core–mantle boundary (CMB) the normal component of displacement $\hat{\mathbf{n}} \cdot \mathbf{s}$ needs to be continuous and the traction $\hat{\mathbf{n}} \cdot \mathbf{T}$ at the bottom of the mantle needs to match the traction $-p\hat{\mathbf{n}}$ at the top of the outer core, where p denotes the perturbed pressure in the fluid.

The weak form of the equation of motion eq. (7) is obtained by taking the dot product with an arbitrary test vector $\mathbf{w}$, integrating by parts over the volume M of the mantle and crust, and imposing the stress-free surface boundary condition. Using the definition (5), this gives

$$\int_M \rho\mathbf{w} \cdot \partial_t^2 \mathbf{s} \, d^3\mathbf{r} + \int_M 2\rho\mathbf{w} \cdot (\boldsymbol{\Omega} \times \partial_t \mathbf{s}) \, d^3\mathbf{r}$$
$$= -\int_M \nabla\mathbf{w} : (\mathbf{T} + \mathbf{G}) \, d^3\mathbf{r} + \mathbf{M} : \nabla\mathbf{w}(\mathbf{r}_s)S(t)$$
$$+ \int_{CMB} p\hat{\mathbf{n}} \cdot \mathbf{w} \, d^2\mathbf{r} - \int_M \rho\mathbf{s} \cdot \mathbf{H} \cdot \mathbf{w} \, d^3\mathbf{r}, \tag{8}$$

where we have used the continuity of traction at the CMB, and where we have defined the second-order tensor

$$\mathbf{G} = \rho[\mathbf{s}\mathbf{g} - (\mathbf{s} \cdot \mathbf{g})\mathbf{I}]. \tag{9}$$

Because of the non-symmetric nature of $\mathbf{G}$, we note that our definition of the double dot product between two second-order tensors $\mathbf{A}$ and $\mathbf{B}$ is $\mathbf{A} : \mathbf{B} = A_{ij} B_{ij}$. Let us mention that it is possible to obtain a symmetric weak formulation of the gravity terms (Chaljub 2000), but this is more expensive from a numerical perspective since one can show that the number of computations is roughly doubled. This is not necessary in finite-element or spectral-element methods, which can handle non-symmetric terms.

3.3 Outer core

In the fluid outer core, making the Cowling approximation, the equation of motion may be written in the form

$$\rho(\partial_t^2 \mathbf{s} + 2\mathbf{\Omega} \times \partial_t \mathbf{s}) = \nabla(\kappa\nabla \cdot \mathbf{s} + \rho\mathbf{s} \cdot \mathbf{g}) - \nabla \cdot (\rho\mathbf{s})\mathbf{g}, \tag{10}$$

where κ denotes the bulk modulus of the fluid. Under the assumption of hydrostatic equilibrium prior to the earthquake, the equation of motion in the fluid may be rewritten in the form

$$\partial_t^2 \mathbf{s} + 2\mathbf{\Omega} \times \partial_t \mathbf{s} = \nabla(\rho^{-1}\kappa\nabla \cdot \mathbf{s} + \mathbf{s} \cdot \mathbf{g}) + \rho^{-1}g^{-2}\kappa(\nabla \cdot \mathbf{s})N^2\mathbf{g}, \tag{11}$$

where $g = |\mathbf{g}|$ and

$$N^2 = (\rho^{-1}\nabla\rho - \rho\kappa^{-1}\mathbf{g}) \cdot \mathbf{g} \tag{12}$$

is the Brunt-Väisälä frequency (e.g. Valette 1986, 1987; Dahlen & Tromp 1998; Chaljub *et al.* 2002). Following the ideas of these authors, we assume that the fluid is stably stratified and isentropic, which means that $N^2 = 0$. Note that this is an approximation since strictly speaking $N^2 \neq 0$ in the PREM outer core. However, it is a very reasonable one, as will be illustrated in Section 4, because it only affects extremely long-period modes confined to the outer core. Using this approximation, the equation of motion in the fluid outer core reduces to

$$\partial_t^2 \mathbf{s} + 2\mathbf{\Omega} \times \partial_t \mathbf{s} = \nabla(\rho^{-1}\kappa\nabla \cdot \mathbf{s} + \mathbf{s} \cdot \mathbf{g}). \tag{13}$$

Next, we introduce a scalar potential χ such that the fluid pressure $p = -\kappa\nabla \cdot \mathbf{s}$ may be written as

$$p = -\rho\partial_t\chi + \rho\mathbf{g} \cdot \mathbf{s}, \tag{14}$$

and we define a vector $\mathbf{u}$ such that

$$\partial_t \mathbf{s} = \nabla\chi + \mathbf{u}. \tag{15}$$

Note that the scalar potential χ introduced in Paper I is a particular case of eqs (14) and (15) in the absence of gravity and rotation. Upon differentiating eq. (14) with respect to time and using eq. (15) we obtain the scalar wave equation

$$\kappa^{-1}\rho\partial_t^2\chi = \nabla \cdot (\nabla\chi + \mathbf{u}) + \kappa^{-1}\rho\mathbf{g} \cdot (\nabla\chi + \mathbf{u}). \tag{16}$$

Substitution of eqs (15) and (14) in eq. (13) yields a precession equation for $\mathbf{u}$:

$$\partial_t \mathbf{u} + 2\mathbf{\Omega} \times \mathbf{u} = -2\mathbf{\Omega} \times \nabla\chi. \tag{17}$$

Let us write the angular rotation vector $\mathbf{\Omega}$ as $\mathbf{\Omega} = \Omega\hat{\mathbf{z}}$. Then the solution to eq. (17) may be written in the form

$$\mathbf{u} = [A\cos(2\Omega t) + B\sin(2\Omega t)]\hat{\mathbf{x}} + [-A\sin(2\Omega t) + B\cos(2\Omega t)]\hat{\mathbf{y}}, \tag{18}$$

where the coefficients A and B are determined by

$$\begin{aligned} \partial_t A &= 2\Omega[\cos(2\Omega t)\partial_y\chi + \sin(2\Omega t)\partial_x\chi], \\ \partial_t B &= 2\Omega[\sin(2\Omega t)\partial_y\chi - \cos(2\Omega t)\partial_x\chi]. \end{aligned} \tag{19}$$

Note that the vector $\mathbf{u}$ has no z-component, i.e. $\hat{\mathbf{z}} \cdot \mathbf{u} = 0$.

In the absence of rotation, eq. (16) reduces to

$$\kappa^{-1}\rho\partial_t^2\chi = \nabla^2\chi + \kappa^{-1}\rho\mathbf{g} \cdot \nabla\chi. \tag{20}$$

Finally, if we ignore the effect of self-gravitation, we obtain

$$\kappa^{-1}\rho\partial_t^2\chi = \nabla^2\chi. \tag{21}$$

Note that this equation, written in the strong form, is different from (I.21) in Paper I, because of the gradient of ρ^{-1}. However, in the numerical implementation of the weak form, after integration by parts, the two forms are equivalent because the mass matrix is exactly diagonal in the SEM.

The weak form of eq. (16) is obtained by multiplying by an arbitrary test function w and integrating by parts, using the continuity of the normal component of velocity:

$$\begin{aligned} \int_{OC} \kappa^{-1}\rho w\partial_t^2\chi \, d^3\mathbf{r} = &-\int_{OC} (\nabla w) \cdot (\nabla\chi + \mathbf{u}) \, d^3\mathbf{r} \\ &+ \int_{OC} \kappa^{-1}\rho w\mathbf{g} \cdot (\nabla\chi + \mathbf{u}) \, d^3\mathbf{r} \\ &+ \int_{CMB} w\hat{\mathbf{n}} \cdot \partial_t\mathbf{s} \, d^2\mathbf{r} - \int_{ICB} w\hat{\mathbf{n}} \cdot \partial_t\mathbf{s} \, d^2\mathbf{r}. \end{aligned} \tag{22}$$

In the domain decomposition between the fluid outer core and the solid inner core and mantle, we match the normal component of velocity by taking $\hat{\mathbf{n}} \cdot \partial_t\mathbf{s}$ at the bottom of the mantle and using it in the surface integral over the CMB in eq. (22), and by taking $\hat{\mathbf{n}} \cdot \partial_t\mathbf{s}$ from the top of the inner core and using it in the surface integral over the ICB in eq. (22). This is identical to the fluid/solid domain decomposition approach adopted in Paper I. The continuity of traction is honoured by calculating the fluid pressure p from eq. (14) based upon $\partial_t\chi$ in the fluid and the normal component of displacement $\hat{\mathbf{n}} \cdot \mathbf{s}$ taken from the solid at the bottom of the mantle (CMB) or at the top of the inner core (ICB). This fluid pressure is then used in the surface integral over the CMB in eq. (8) and in the surface integral over the ICB in eq. (23).

3.4 Inner core

The weak form of the equation of motion in the solid inner core is similar to eq. (8):

$$\begin{aligned} \int_{IC} \rho\mathbf{w} \cdot \partial_t^2\mathbf{s} \, d^3\mathbf{r} + \int_{IC} 2\rho\mathbf{w} \cdot (\mathbf{\Omega} \times \partial_t\mathbf{s}) \, d^3\mathbf{r} \\ = -\int_{IC} \nabla\mathbf{w} : (\mathbf{T} + \mathbf{G}) \, d^3\mathbf{r} - \int_{ICB} p\hat{\mathbf{n}} \cdot \mathbf{w} \, d^2\mathbf{r} \\ - \int_{IC} \rho\mathbf{s} \cdot \mathbf{H} \cdot \mathbf{w} \, d^3\mathbf{r}. \end{aligned} \tag{23}$$

Note that the inner core–outer core interactions, represented by the surface integrals over the ICB in eqs (22) and (23), also honour continuity in traction and continuity of the normal components of displacement and velocity.

3.5 Complications owing to the oceans

Those areas of the Earth that are covered by a water layer (oceans or large lakes) are subject to a slightly more complicated weak

formulation of the problem. The weak form of the equations of motion in the solid Earth (mantle and crust) covered by water is

$$\int_M \rho \mathbf{w} \cdot \partial_t^2 \mathbf{s}\, d^3\mathbf{r} + \int_M 2\rho \mathbf{w} \cdot (\mathbf{\Omega} \times \partial_t \mathbf{s})\, d^3\mathbf{r}$$

$$= - \int_M \nabla \mathbf{w} : (\mathbf{T} + \mathbf{G})\, d^3\mathbf{r} + \mathbf{M} : \nabla \mathbf{w}(\mathbf{r}_s) S(t)$$

$$+ \int_{CMB} p\hat{\mathbf{n}} \cdot \mathbf{w}\, d^2\mathbf{r} - \int_{OCB} p\hat{\mathbf{n}} \cdot \mathbf{w}\, d^2\mathbf{r} - \int_M \rho \mathbf{s} \cdot \mathbf{H} \cdot \mathbf{w}\, d^3\mathbf{r},$$

$$(24)$$

where OCB denotes the ocean-crust boundary (i.e. the ocean floor). What we need is an expression for the fluid pressure p at the OCB. In the oceans, the waves satisfy the fluid wave eq. (13), which can be rewritten as

$$\partial_t^2 \mathbf{s} + 2\mathbf{\Omega} \times \partial_t \mathbf{s} = -\nabla(\rho^{-1} p - \mathbf{s} \cdot \mathbf{g}). \tag{25}$$

We shall assume that the oceans are incompressible, which means that the entire water column moves as a whole as a result of the normal displacement $\hat{\mathbf{n}} \cdot \mathbf{s}$ of the seafloor. This is a good approximation at the periods considered in this study, as will be demonstrated in Section 4, because the thickness of the oceans is small compared with the wavelength of the seismic waves we are interested in. This would cease to be true at very short periods, typically below roughly 5 s. We only wish to reproduce the effect of the load at the ocean floor, not phases that actually propagate in the oceans themselves (e.g. the tsunami).

Suppose that the water column has a local thickness h. Upon integrating eq. (25) over the water column, taking into account the variations of gravity with radius according to eq. (1), we obtain the local result

$$p = \rho_w h \hat{\mathbf{n}} \cdot \partial_t^2 \mathbf{s} + 2\rho_w h \hat{\mathbf{n}} \cdot (\mathbf{\Omega} \times \partial_t \mathbf{s}) + 4\pi G \rho_w^2 h \hat{\mathbf{n}} \cdot \mathbf{s}, \tag{26}$$

where ρ_w denotes the density of sea water ($\rho_w \simeq 1020$ kg m^{-3}). As a result, the weak form of the equations of motion in the crust and mantle eq. (24) becomes

$$\int_M \rho \mathbf{w} \cdot \partial_t^2 \mathbf{s}\, d^3\mathbf{r} + \int_{OCB} \rho_w h(\mathbf{w} \cdot \hat{\mathbf{n}})\left(\hat{\mathbf{n}} \cdot \partial_t^2 \mathbf{s}\right) d^2\mathbf{r}$$

$$+ \int_M 2\rho \mathbf{w} \cdot (\mathbf{\Omega} \times \partial_t \mathbf{s})\, d^3\mathbf{r} + \int_{OCB} 2\rho_w h(\mathbf{w} \cdot \hat{\mathbf{n}})[\hat{\mathbf{n}} \cdot (\mathbf{\Omega} \times \partial_t \mathbf{s})]\, d^2\mathbf{r}$$

$$= - \int_M \nabla \mathbf{w} : (\mathbf{T} + \mathbf{G})\, d^3\mathbf{r} + \mathbf{M} : \nabla \mathbf{w}(\mathbf{r}_s) S(t) - \int_M \rho \mathbf{s} \cdot \mathbf{H} \cdot \mathbf{w}\, d^3\mathbf{r}$$

$$+ \int_{CMB} p\hat{\mathbf{n}} \cdot \mathbf{w}\, d^2\mathbf{r} - \int_{OCB} 4\pi G \rho_w^2 h(\hat{\mathbf{n}} \cdot \mathbf{w})(\hat{\mathbf{n}} \cdot \mathbf{s})\, d^2\mathbf{r}. \tag{27}$$

In practice, the ocean load represents a small effect, and the gravity and rotation terms in eq. (26) involve additional small corrections that can be safely neglected. Hence we solve the following equation in the mantle, moving the Coriolis term to the right-hand side:

$$\int_M \rho \mathbf{w} \cdot \partial_t^2 \mathbf{s}\, d^3\mathbf{r} + \int_{OCB} \rho_w h(\mathbf{w} \cdot \hat{\mathbf{n}})\left(\hat{\mathbf{n}} \cdot \partial_t^2 \mathbf{s}\right) d^2\mathbf{r}$$

$$= - \int_M 2\rho \mathbf{w} \cdot (\mathbf{\Omega} \times \partial_t \mathbf{s})\, d^3\mathbf{r} - \int_M \nabla \mathbf{w} : (\mathbf{T} + \mathbf{G})\, d^3\mathbf{r}$$

$$+ \mathbf{M} : \nabla \mathbf{w}(\mathbf{r}_s) S(t) - \int_M \rho \mathbf{s} \cdot \mathbf{H} \cdot \mathbf{w}\, d^3\mathbf{r} + \int_{CMB} p\hat{\mathbf{n}} \cdot \mathbf{w}\, d^2\mathbf{r}.$$

$$(28)$$

The local thickness of the oceans, h, is taken from a bathymetry map, as explained in Section 2 (see Fig. 5). Note that this means that

we can very efficiently take into account the effects of the oceans by a simple modification of the mass matrix for the points (more precisely the degrees of freedom) located at the ocean floor, as can be concluded from the second term on the left-hand side of eq. (28), which is a mere surface integral along the OCB. Note also that the compressional-wave velocity in the oceans does not appear in eqs (27) and (28).

3.6 Discretization and time marching

Most of the terms in the weak formulations eqs (8), (22), (23) and (28) were presented in Paper I. In this section we give explicit expressions for the elemental form of the terms that arise as a result of the Earth's rotation and self-gravitation in the context of the Cowling approximation.

The weak form of the Coriolis term in eqs (8), (23) and (28) for an element Ω_e is

$$\int_{\Omega_e} 2\rho \mathbf{w} \cdot (\mathbf{\Omega} \times \partial_t \mathbf{s})\, d^3\mathbf{r} \approx 2\Omega \sum_{\alpha,\beta,\gamma=0}^{n} \omega_\alpha \omega_\beta \omega_\gamma J^{\alpha\beta\gamma} \rho^{\alpha\beta\gamma}$$

$$\times \sum_{i,j=1}^{3} w_i^{\alpha\beta\gamma} \epsilon_{i3j} \dot{s}_j^{\alpha\beta\gamma}. \tag{29}$$

Here $J^{\alpha\beta\gamma}$ is the Jacobian evaluated at the Gauss–Lobatto–Legendre points, $\omega_\alpha > 0$, for $\alpha = 0, \ldots, n$, denote the weights associated with the Gauss–Lobatto–Legendre quadrature (Canuto *et al.* 1988, p. 61), and ϵ_{ijk} is the alternating tensor. We have used the expansions (I.31) and (I.32) of Paper I for the displacement field $\mathbf{s}$ and the test vector $\mathbf{w}$. Note that the Coriolis matrix eq. (29) is diagonal and has no contribution in the z-direction.

Self-gravitation in the context of the Cowling approximation contributes two terms to eqs (8) and (23). The first contribution can be incorporated in the calculation of the stiffness matrix by making the substitution $\mathbf{T} \to \mathbf{T} + \mathbf{G}$, remembering that $\mathbf{G}$ is non-symmetric. The second gravity contribution has the weak form

$$\int_{\Omega_e} \rho \mathbf{s} \cdot \mathbf{H} \cdot \mathbf{w}\, d^3\mathbf{r} \approx \sum_{\alpha,\beta,\gamma=0}^{n} \omega_\alpha \omega_\beta \omega_\gamma J^{\alpha\beta\gamma} \rho^{\alpha\beta\gamma}$$

$$\times \sum_{i,j=1}^{3} w_i^{\alpha\beta\gamma} H_{ij}^{\alpha\beta\gamma} s_j^{\alpha\beta\gamma}. \tag{30}$$

Note that this gravity term is diagonal.

The only new fluid term that arises in the context of self-gravitation and rotation is

$$\int_{\Omega_e} \kappa^{-1} \rho w \mathbf{g} \cdot (\nabla \chi + \mathbf{u})\, d^3\mathbf{r} \approx \sum_{\alpha,\beta,\gamma=0}^{n} \omega_\alpha \omega_\beta \omega_\gamma J^{\alpha\beta\gamma} w^{\alpha\beta\gamma} (\kappa^{-1}\rho)^{\alpha\beta\gamma}$$

$$\times \sum_{i=1}^{3} g_i^{\alpha\beta\gamma}\left[(\partial_i \chi)^{\alpha\beta\gamma} + u_i^{\alpha\beta\gamma}\right], \tag{31}$$

where $(\partial_i \chi)^{\alpha\beta\gamma}$ is given by (I.45) in Paper I.

Schematically, the global system of equations we need to solve may be written in the form

$$\mathbf{M\ddot{U} + W\dot{U} + KU + BU = F}, \tag{32}$$

where $\mathbf{U}$ denotes the displacement vector at all gridpoints in the global mesh, $\mathbf{M}$ the global diagonal mass matrix, $\mathbf{W}$ the global Coriolis matrix, $\mathbf{K}$ the global stiffness matrix, $\mathbf{B}$ the boundary interactions at the CMB and the ICB and $\mathbf{F}$ the source term.

The presence of an ocean layer, in the context of the equivalent ocean load formulation introduced above, only affects the normal component of displacement at the ocean floor, i.e. at the top of the mesh. All that needs to be done for these points is to replace the mass matrix M by $M + m$, where m denotes the 'surface mass' that represents the ocean load. This modified mass matrix remains globally diagonal, and inverting it involves a simple division.

The presence of rotation is taken into account in the solid regions by adding the contribution of the Coriolis force, which is a straightforward modification of the SEM algorithm since the term is diagonal, which means that it can be added directly to the x and y components of acceleration in eq. (32) at the global level, after assembly of the system. In the outer core we need to keep track of the coefficients A and B by marching eq. (19). This contribution turns out to be extremely small, but is included in this study for completeness.

In Paper I the momentum eq. (32) was marched using a classical explicit second-order finite-difference scheme, which is a particular case of the general Newmark scheme for hyperbolic equations (e.g. Hughes 1987). In order to perform the coupling between solid and fluid regions in the domain decomposition approach, the scheme is implemented in a staggered predictor–multicorrector format, following the ideas of Park & Felippa (1980) and Felippa & Deruntz (1984). In addition, in Paper I the memory variable equations used to mimic attenuation with a constant quality factor Q were marched separately using a modified second-order Runge–Kutta scheme. In this paper, we still make use of these two schemes, but in addition we need to march the precession eq. (19). A second-order Runge–Kutta scheme could be used for this purpose, but considering that the rotation rate of the Earth is slow compared with the timescale of wave propagation, we instead use a simple Euler time-integration scheme. The properties of the time schemes, as well as the value of the time step Δt, are unchanged with respect to Paper I.

4 NUMERICAL RESULTS

In this section we first carefully benchmark the implementations of self-gravitation and the oceans for the spherically symmetric model PREM by comparing the SEM results with the normal-mode solution (e.g. Dahlen & Tromp 1998). Subsequently, we study the effects of rotation on surface waves based upon a south–north propagation path, which is susceptible to Coriolis coupling. In the last part of this section we combine the effects of self-gravitation, the oceans, rotation, anisotropy and attenuation with a 3-D mantle model, a 3-D crustal model, ellipticity, topography and bathymetry to simulate two real earthquakes in Vanuatu and Bolivia.

All of the calculations in this section incorporate an anisotropic asthenosphere as in PREM (the upper 220 km of the Earth's mantle). Attenuation is included in the Vanuatu and Bolivia calculations, but not in the tests for self-gravitation, the oceans and rotation, in order to validate these effects individually. Anisotropy and attenuation in the context of the SEM were validated in Paper I. The normal-mode and SEM calculations also include self-gravitation based upon the Cowling approximation, unless explicitly stated otherwise. We use the same time integration and mesh parameters as in Paper I, i.e. $N = 240$ spectral elements at the surface in each direction for each of the six chunks of the cubed sphere mesh, a time step of $\Delta t = 0.20$ s and a Heaviside source time-function. The results are subsequently convolved with a Gaussian function with a half-duration of 18 s in

the case of the validation tests and for the Vanuatu earthquake, and 15 s in the case of the Bolivia earthquake (see Fig. I.12 in Paper I). The full mesh has roughly 180 million global points (corresponding to approximately 483 million degrees of freedom, since we solve for the three components of displacement at each gridpoint, except in the fluid outer core, where we solve for the scalar potential), and the calculations are performed on a 151-processor PC cluster with 76 Gb of memory.

4.1 Validation of self-gravitation in Cowling approximation

First, let us illustrate the magnitude of the gravitational contributions. We compare the results of an SEM calculation without gravity with the normal-mode solution with the full implementation of self-gravitation. Because the influence of gravity is mainly noticeable at long periods (typically greater than 100 s), for this test we convolve the synthetics with a Gaussian function with a half-duration of 18 s and low-pass filter the results at a corner period of 120 s using a six-pole two-pass Butterworth filter. We choose a record length of 2 hours in order to include R_1 and G_1–G_2. In Fig. 6 we show the results at an epicentral distance of $100°$ for a large shallow $M_w = 8.2$ event at a depth of 15 km (the Irian Jaya earthquake of Paper I, see Figs I.13–18). At these long periods there is a large effect associated with gravity on the vertical and longitudinal components, whereas the transverse component is unaffected. The fact that the fit with normal modes is perfect on the transverse component demonstrates that the SEM synthetics in the absence of gravity are very accurate. Closer to the antipode, self-gravitation has a small effect on the transverse component because the spheroidal motion has a small transverse component (Dahlen & Tromp 1998), as illustrated in Fig. 7.

Next, we demonstrate that the Cowling approximation eq. (7) is a good approximation of the full equations of motion eq. (6). The normal-mode calculation software has the ability to compute catalogues with full gravity as well as in the Cowling approximation. In Fig. 8, we show the vertical and longitudinal components of displacement at an epicentral distance of $100°$ for the shallow Irian Jaya event. The solid lines are synthetics that incorporate perturbations in the gravitational potential, and the dotted lines are synthetics calculated based upon the Cowling approximation. The agreement between the two curves is very good, which shows that the Cowling approximation is satisfactory and can generally be safely used in global seismology. We do not show the transverse component of displacement because it is not affected by gravity.

Finally, we show that the implementation of self-gravitation in the SEM based upon the Cowling approximation eqs (8), (22) and (23) is accurate. As mentioned earlier, the implementation of self-gravitation in the context of the SEM was studied by Chaljub (2000). We adopt a similar approach here, except that we use a simpler non-symmetric form as explained in Section 3. In Fig. 9 we compare the SEM results with the normal-mode solution in the Cowling approximation for the shallow Irian Jaya event at an epicentral distance of $100°$. We focus on multiorbit surface waves up to R_4 and G_5 at long periods. Compared with Fig. 6, we fit the large signal owing to gravity very well, as is confirmed by the close-up on the vertical component in Fig. 10. The SEM synthetics are very accurate even for R_4 and G_5. R_3 and R_4 exhibit weak numerical dispersion, while G_5 is perfectly reproduced. Because the mode synthetics are only quasi-analytical, and therefore contain some numerical errors (e.g. related to numerical integration and root-finding routines), we do
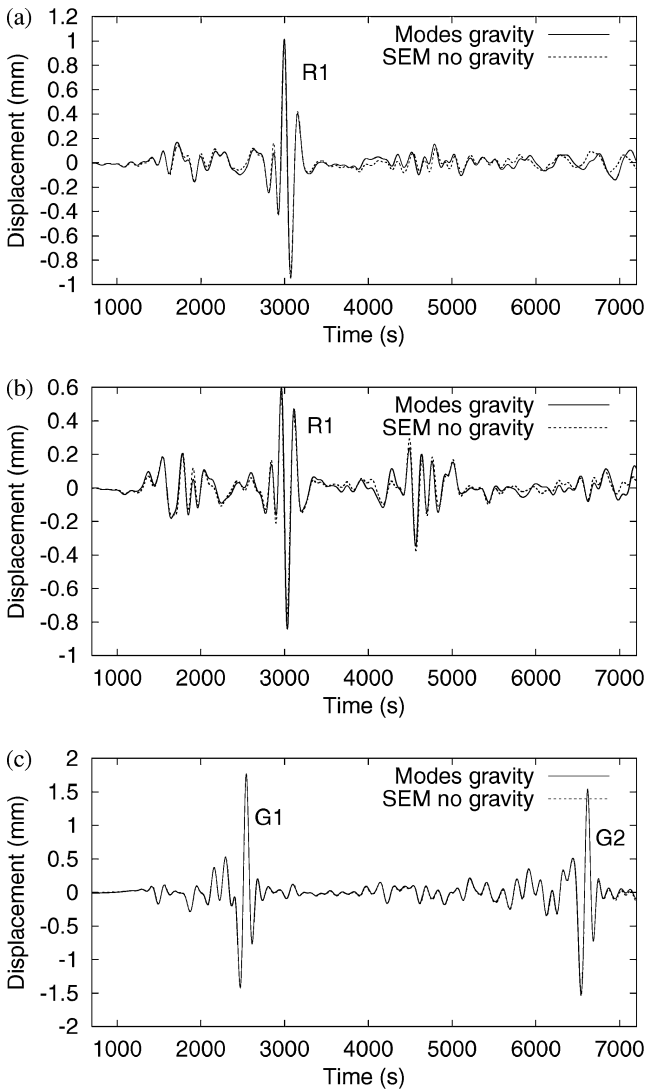
Figure 6. Vertical (top), longitudinal (middle) and transverse (bottom) components of displacement of the normal-mode solution for the shallow Irian Jaya event with the full implementation of gravity (solid line) and the SEM solution without gravity (dotted line) at an epicentral distance of $100°$. The results have been low-pass filtered at a corner period of 120 s. At these long periods there is a large effect owing to gravity on the vertical and longitudinal components. The transverse component is unaffected. The total duration of the simulation is two hours in order to show R_1 and G_1–G_2.

not show the difference between the SEM and normal-mode synthetics, since this is not an objective measure of the accuracy of the SEM. Note that in Fig. 9, the normal-mode reference is based upon the Cowling approximation, while it is based upon the full implementation of gravity in Fig. 6, but we know from Fig. 8 that the two normal-mode results agree very well. Fig. 10 also validates the $N^2 = 0$ approximation used in eq. (13) since our SEM results fit the normal-mode calculation for PREM without the $N^2 = 0$ assumption very well. Note also that attenuation is not included in this simulation, therefore the amplitude of the multiorbit surface waves decays more slowly.

At higher frequencies, the main effect of gravity for shallow events is to slow down the Rayleigh wave slightly, as observed by Chaljub (2000). To illustrate this, in Fig. 11 we show the original results (i.e. the results for the Gaussian source with a half-duration
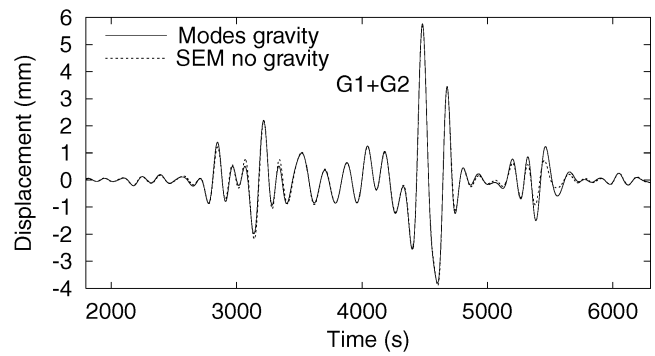
Figure 7. Transverse component of displacement of the PREM normal-mode solution for the shallow Irian Jaya event with the full implementation of gravity (solid line) and the SEM solution without gravity (dotted line) at an epicentral distance of $178°$. At these long periods, close to the antipode the transverse motion has a small spheroidal component (Dahlen & Tromp 1998). Therefore, self-gravitation has a small effect on the transverse component. Note that G_1 and G_2 are almost completely superimposed.

of 18 s, before filtering at 120 s) at an epicentral distance of $60°$ for the vertical component of displacement. In the absence of self-gravitation the Rayleigh wave is faster than in the Cowling approximation. When we introduce self-gravitation in the SEM we fit most of the discrepancy. A small phase shift remains in the coda of the Rayleigh wave; this is attributed to a slight mesh subsampling that induces numerical dispersion in the SEM results.
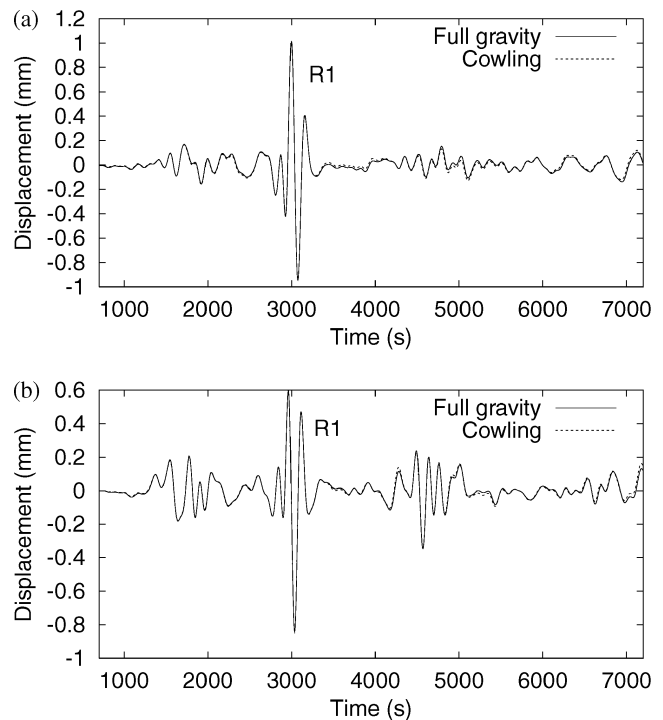
Figure 8. Vertical (top) and longitudinal (bottom) components of PREM normal-mode synthetics with the full implementation of gravity (solid line) and in the Cowling approximation (dotted line) for a shallow event at an epicentral distance of $100°$. Compared with Fig. 6, the agreement between the two curves is satisfactory, which shows that the Cowling approximation is a good approximation of full gravity.
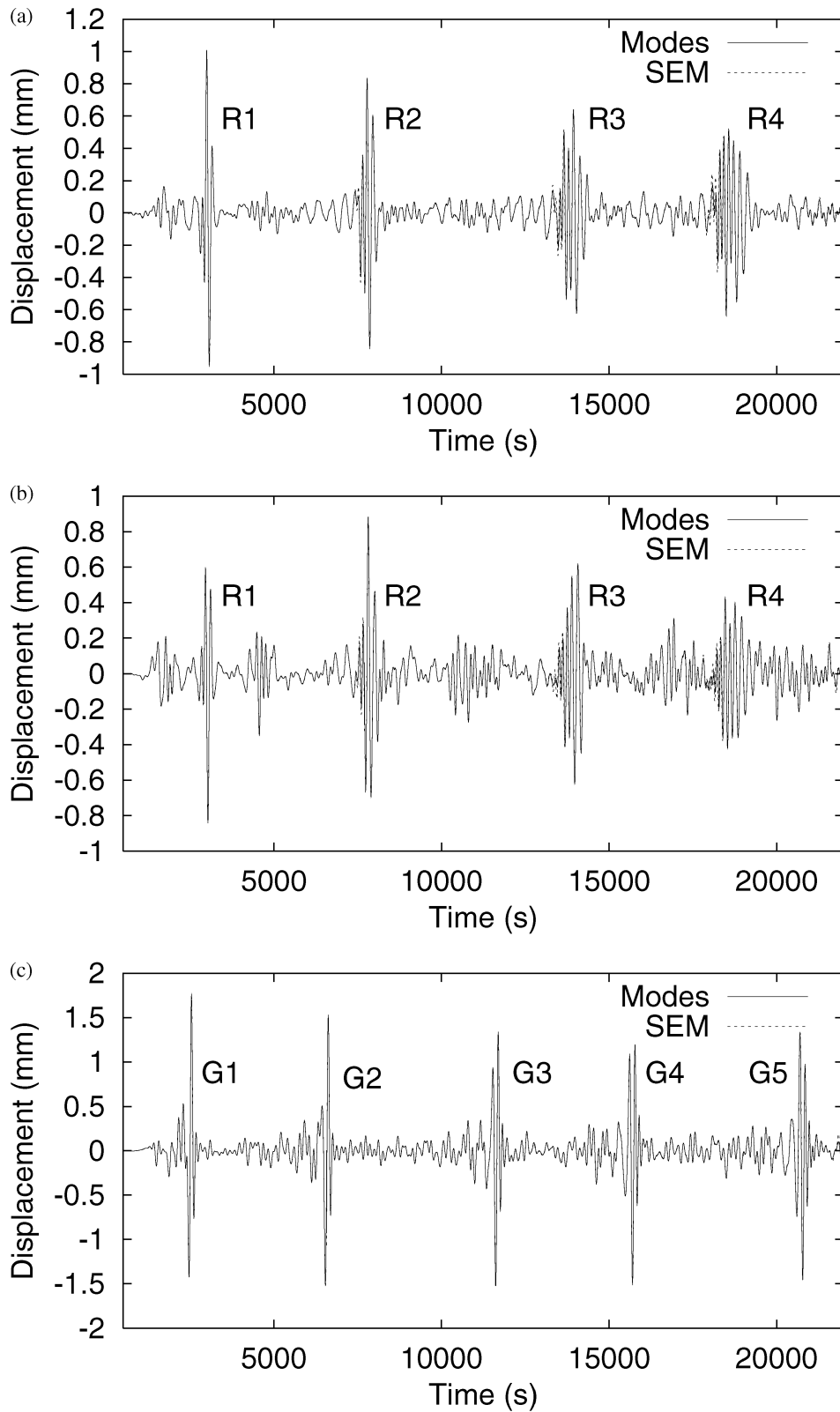
Figure 9. Vertical (top), longitudinal (middle) and transverse (bottom) components of the PREM normal-mode solution in the Cowling approximation (solid line) compared with the SEM displacement (dotted line) for the shallow Irian Jaya event at an epicentral distance of $100°$. One can observe the multiorbit surface waves up to R_4 and G_5, which are very accurately matched. R_3 and R_4 exhibit very weak numerical dispersion, while G_5 is perfectly reproduced. We have low-pass filtered the results at a corner period of 120 s. Compared with Fig. 6 we fit the large gravitational signal very well, as is confirmed by the close-up on the vertical component in Fig. 10. The transverse component is not affected by gravity. Note that attenuation is not included in this simulation; therefore the amplitude of the multiorbit surface waves decays more slowly.
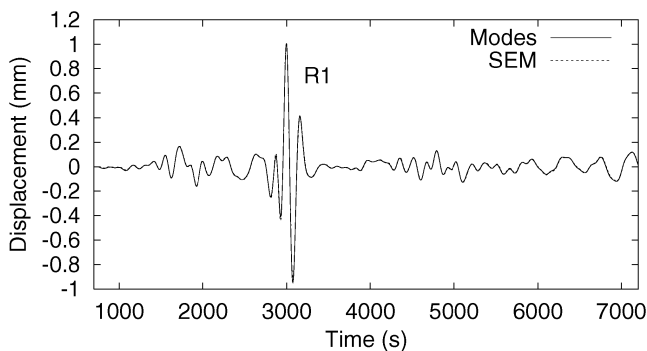
Figure 10. Close-up on the vertical component (Fig. 9) of the PREM normal-mode solution in the Cowling approximation (solid line) and the SEM displacement (dotted line) for the shallow Irian Jaya event at an epicentral distance of 100°. We have low-pass filtered the results at a corner period of 120 s. Compared with Fig. 6 we fit the large gravitational signal very well.
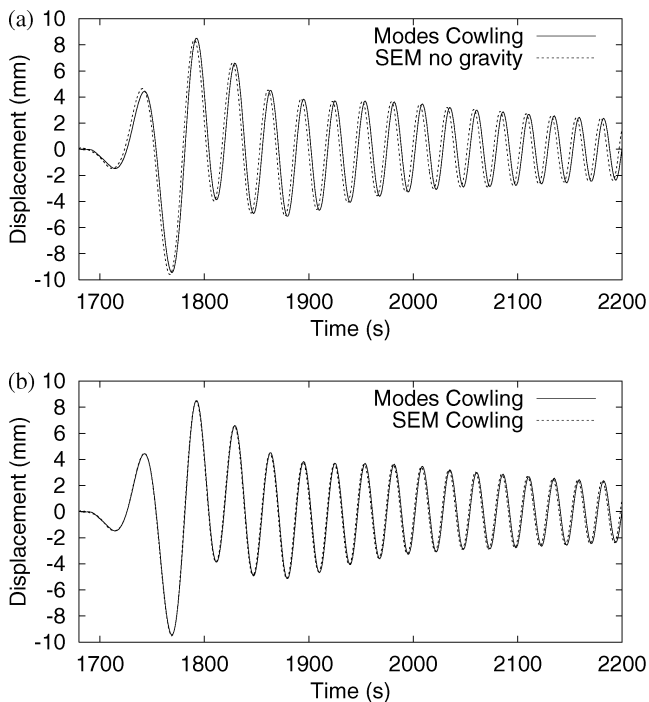
Figure 11. Vertical component of displacement for a PREM normal-mode calculation in the Cowling approximation (solid line) compared with the SEM result in the absence of gravity (top, dotted line) and the SEM result based upon the Cowling approximation (bottom, dotted line). The results are for the shallow Irian Jaya earthquake using a Gaussian source with a half-duration of 18 s. In the absence of self-gravitation the Rayleigh wave arrives earlier. When we introduce self-gravitation in the SEM we fit most of the discrepancy. A small phase shift remains in the coda of the Rayleigh wave; this is attributed to a slight mesh subsampling, which induces numerical dispersion in the SEM results.

4.2 Effects of the oceans

The presence of the oceans is mostly relevant for the dispersion of Rayleigh waves in the case of shallow events, as well as for free-surface reflected phases, such as *PP*, *SS* and *SP*. To illustrate the magnitude of the effect of the oceans on wave propagation, Fig. 12 shows results of an SEM calculation for PREM without the ocean layer (therefore using an Earth radius of 6368 km instead of
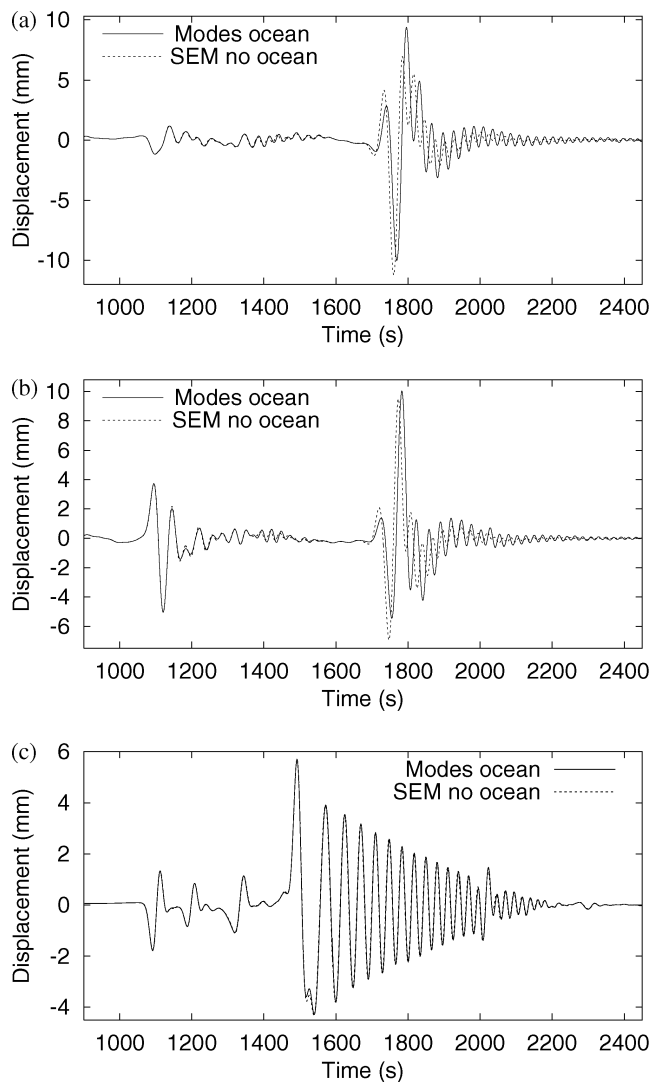
Figure 12. Vertical (top), longitudinal (middle) and transverse (bottom) components of displacement for a PREM normal-mode calculation with a 3 km-thick ocean layer (solid line) and for the SEM without the ocean layer (dotted line). The results are for the shallow Irian Jaya earthquake recorded at an epicentral distance of 60°. The Gaussian source has a half-duration of 25 s. The oceans have a small effect on *P* and *S* multiples and a large effect on the Rayleigh wave, which is slowed down considerably. The dispersion of the Rayleigh wave also changes dramatically. The Love wave is not affected by the presence of the oceans.

6371 km), compared with the PREM normal-mode solution computed with the ocean layer. The event is the shallow Irian Jaya earthquake, and the station is located at the ocean floor at an epicentral distance of 60°. The Gaussian source has a half-duration of 25 s. The oceans have a small effect on *P* and *S* multiples and a large effect on the Rayleigh wave, which is slowed down significantly. The dispersion of the Rayleigh wave also changes dramatically. The Love wave is not affected by the presence of the oceans.

The most intuitive way to incorporate the effect of the oceans in the SEM is by defining a mesh of fluid elements, just as we do for the outer core. In principle, we can couple the ocean and crustal regions in the SEM based upon a domain-decomposition algorithm, as we do for the outer core at the ICB and the CMB (see Paper I for details). Unfortunately, closer examination reveals that the problem

is much more challenging than it appears. First, the compressional-wave velocity in the oceans ($\simeq$1.45 km s^{-1}) is much smaller than the smallest shear-wave velocity in the PREM crust ($\simeq$3.2 km s^{-1}). Therefore, in order to maintain a similar number of grid points per wavelength throughout the mesh, we would need far more points in the lateral direction in the oceans than in the crust (typically twice as many since $3.2/1.45 \simeq 2$). Because the crust is already the region of the mesh that has the highest density of elements, adding ocean elements would be very expensive in terms of memory and CPU requirements. Additionally, as at the ICB and the CMB, we would need to iterate the time scheme to couple the oceans and the crust in the domain decomposition, thereby increasing the CPU requirements even more. Because the oceans are very thin compared with the rest of the model (an average ocean thickness of 3 km compared with an average crustal thickness of 21 km and an Earth radius of 6371 km), the aspect ratio (i.e. the ratio of the lateral to the radial dimensions of the elements) of these ocean elements would be very large. This often induces stability problems in the time scheme in finite-element methods (e.g. Hughes 1987). Another drawback of meshing the oceans explicitly is that we would need to impose a minimum radial size (i.e. thickness) for the elements, typically 3 km, in order to avoid stability problems (the time step Δt tends to zero when the element size tends to zero), and therefore we could not handle shallow oceans.

Because we would roughly need to double the number of elements in the oceans relative to the crust, we could no longer use a geometrically conforming mesh, and would need to turn to a non-conforming mesh. This introduces several theoretical, numerical and practical complications. The general framework for non-conforming finite-element approximations is called the 'mortar' method (Bernardi *et al.* 1990, 1994; Chaljub *et al.* 2002). In simple geometrical cases, straightforward implementations that are particular cases of the mortar method can be used (Rønquist 1996; Kopriva 1996). For our problem, the easiest implementation is to introduce a mesh of small spectral elements in the oceans, the corners of which are the Gauss–Lobatto–Legendre points of a larger spectral element in the crust, as illustrated in Fig. 13. This is a particular case of the least-squares matching method of Kopriva (1996), which in turn can be seen as a particular case of the mortar method. In this approach one matches the two subdomains based upon a surface integral in which the fields at the contact between the fluid and solid regions are projected based upon a least-squares algorithm.

In Section 3 we mentioned that by assuming that the oceans are incompressible, which is a reasonable approximation considering the fact that the thickness of the oceans is much smaller than the
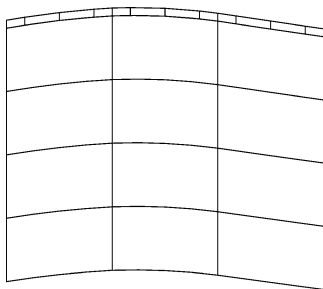
Figure 13. Geometrically non-conforming mesh that can be used to implement the ocean coupling technique based upon the least-squares method of Kopriva (1996). The corners of the small fluid spectral elements in the oceans correspond to the Gauss–Lobatto–Legendre points of the larger spectral elements in the crust. These points are non-evenly spaced (e.g. Canuto *et al.* 1988).
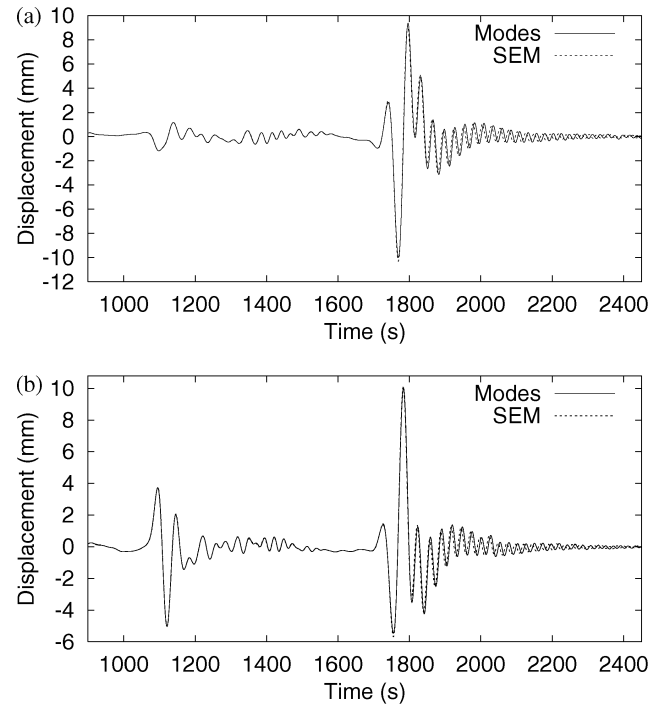
Figure 14. Vertical (top) and longitudinal (bottom) components of displacement for a PREM normal-mode calculation with a 3 km-thick ocean layer (solid line) and for the SEM with the same ocean layer (dotted line). The results are for the shallow Irian Jaya earthquake recorded at an epicentral distance of 60°. The Gaussian source has a half-duration of 25 s. Compared with Fig. 12, we fit the small effect of the oceans on *P* and *S* multiples perfectly, and most of the large effect on the Rayleigh wave, which is slowed down significantly and has a different dispersion. The small discrepancy in the coda of the Rayleigh wave is mainly attributed to the approximate ocean load formulation of eq. (28). The transverse component, which is not affected by the presence of the oceans, is not shown.

wavelengths under consideration, we can avoid explicitly meshing the oceans (this would cease to be true at very short periods). Instead, the effect of the oceans is represented by a mere surface integral. In order to assess the validity of this approximation, in Fig. 14 we perform a comparison between the PREM normal-mode solution with an ocean and an SEM simulation with a 3 km ocean introduced as an equivalent load for the same event as in Fig. 12. Compared with Fig. 12, we fit the small effect on *P* and *S* multiples perfectly, and we correctly reproduce most of the effect on the Rayleigh wave, which is slowed down significantly by the oceans. The Love wave, which is not affected by the presence of the oceans, is not shown. There is a small phase shift in the coda of the Rayleigh wave in the SEM results. We attribute this effect to the fact that the ocean load formulation of eq. (28) is approximate. Let us mention that a slight mesh subsampling that induces numerical dispersion in the SEM results might play a role as well. Some of the observed discrepancies might come from the normal-mode solution itself, which is not perfect since it does not include the tsunami branch. However, tests not shown here conducted with the SEM using the least-squares method of Kopriva (1996) based upon the implementation illustrated in Fig. 13 gave results that were slightly closer to the mode solution, therefore we believe that most of the discrepancy comes from the ocean load approximation itself.

Let us finally mention that for very long simulations of several tens of thousands of time steps in tests not presented here we noticed some instability problems with our implementation of the method of

Kopriva (1996), while no problems were encountered for the ocean load formulation. We attribute these long-term instability problems to slowly accumulating errors in the least-squares projection between the non-conforming meshes.

4.3 Effects of the Earth's rotation

As we mentioned in Section 3.6, incorporating the Coriolis force in SEM synthetics involves a trivial modification of the x and y components of acceleration. In contrast, calculating time-domain normal-mode synthetics that fully incorporate rotation is a non-trivial matter, especially at shorter periods, because it involves cross-coupling between spheroidal and toroidal mode branches. Therefore, we compare SEM synthetics with rotation with SEM synthetics without rotation to illustrate the size of this effect. We include ellipticity in the calculations and choose a south–north propagation path for an event located at the South Pole in order to maximize the effects of Coriolis coupling. The effect of rotation is to couple the *P-SV* motion with *SH* motion, and vice versa. Therefore, we expect some transfer of energy between the vertical and longitudinal components and the transverse component. We use the moment tensor of the shallow Irian Jaya event in order to generate a large-amplitude surface wave. In Figs 15 and 16 we show the vertical and transverse components of displacement in the presence and absence of rotation at an epicentral distance of 120° along the Greenwich meridian. We also show the residuals (i.e. the difference between the two results) in a separate panel for clarity. In this case the residuals are meaningful because we
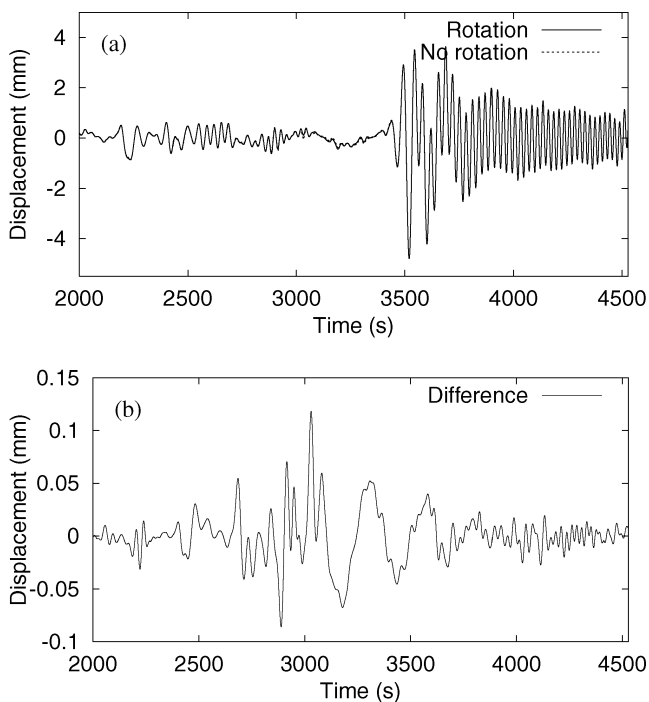
Figure 15. Vertical (top) component of displacement at an epicentral distance of 120° from a shallow event located at the South Pole. The ray paths are south–north and the event generates a large-amplitude surface wave for which we expect Coriolis coupling to be most significant. The SEM results with rotation are represented by the solid line and those without rotation by the dotted line. The residuals (difference between the two results, bottom) show that the effects of rotation can be as large as 3.5 per cent of the maximum amplitude of the surface wave. The large residual at 3000 s coincides with the arrival of the Love wave, which has acquired a vertical component of motion.
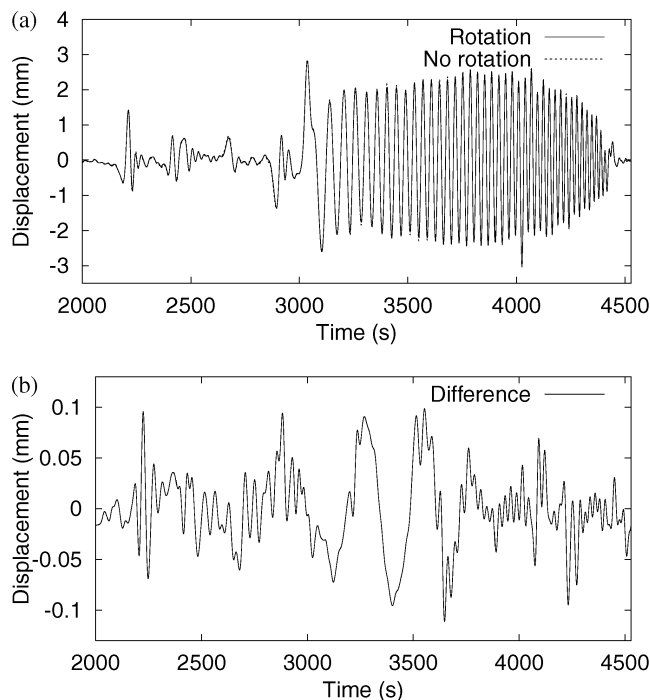
Figure 16. Transverse (top) component of displacement at an epicentral distance of 120° from a shallow event located at the South Pole. The SEM results with rotation are represented by the solid line and those without rotation by the dotted line. The residuals (bottom) show that the effects of rotation can be as large as 3.5 per cent of the maximum amplitude of the surface wave. The effect of rotation on the transverse component shown in this figure should be compared with the effect on the vertical component shown in Fig. 15.

compare SEM synthetics with and without rotation, both of which have very similar numerical dispersion. One can observe that the maximum effect owing to rotation at this station is of the order of 3.5 per cent of the maximum amplitude of the surface wave.

4.4 3-D simulations for two real events

As a final application of the SEM we combine all the complications of a full 3-D Earth model. The simulations presented in this section include anisotropy, attenuation, self-gravitation, the oceans, rotation, ellipticity, topography and bathymetry, a 3-D mantle model and a 3-D crustal model. We first model an event with a moment magnitude $M_w = 7.4$ that occurred on 1999 November 26 in Vanuatu at a depth of 15 km. Its focal mechanism is given in Fig. 17. The source has a half-duration of 18 s. This event gives us the opportunity to study the effects of the thin oceanic crust ($\sim$7 km) and the water layer on surface waves travelling across the Pacific. PREM includes a 3 km thick water layer and has a peculiar crust with a thickness of 21.4 km; therefore we expect a 3-D SEM simulation to fit the data much better. Fig. 18 shows the three components of displacement convolved with the instrument response (which effectively gives ground velocity) and low-pass filtered at a corner frequency of 40 s at station MAJO in Japan, at an epicentral distance of 60°. We use a six-pole two-pass Butterworth filter. Note how the normal-mode synthetics for PREM predict a Love wave with a duration which is much too long, and a Rayleigh wave that arrives much too late. The SEM synthetics incorporate the thin oceanic crust and predict the arrival time of the Rayleigh wave much better, as well as the short duration of the Love wave (although it arrives a bit too early). An
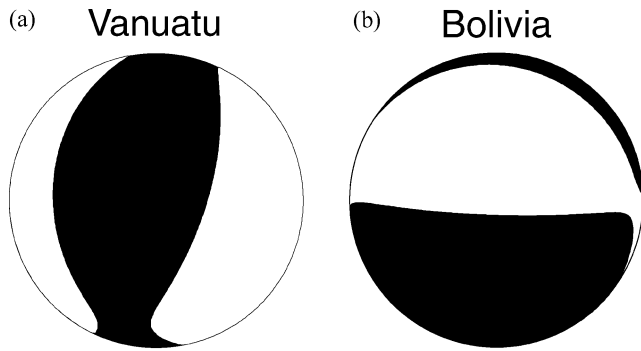
Figure 17. Focal mechanisms for the shallow 1999 November 26, Vanuatu earthquake which occurred at a depth of 15 km and had a moment magnitude $M_w = 7.4$ (left) and the deep 1994 June 9, Bolivia earthquake which occurred at a depth of 647 km and had a moment magnitude $M_w = 8.2$ (right).

even more spectacular example of a fast Rayleigh wave is shown in Fig. 19 for the vertical component of the Pasadena, California, TriNet station PAS, at an epicentral distance of 86°, where the Rayleigh wave arrives 85 s earlier than in PREM. Note that the

3-D SEM synthetic matches this early arrival very nicely and tracks the phase of the Rayleigh wave quite well.

Our next fully 3-D simulation is for a large $M_w = 8.2$ event at a depth of 647 km (the Bolivia earthquake of Paper I, see Figs I.20–24). Its focal mechanism is given in Fig. 17. The source has a half-duration of 15 s. The seismograms are recorded at TriNet station PAS in Pasadena, California, at an epicentral distance of 68°. Again, the SEM synthetics are convolved with the instrument response and low-pass filtered at a corner frequency of 40 s. The fit in Fig. 20 is significantly improved, in particular the large *SKS*, *sSKS* and *SS* phases between 1400 and 1700 s, as well as the Rayleigh wave around 2000 s. The improvement obtained with the 3-D SEM simulation is less spectacular than in Figs 18 and 19 because the fit based upon PREM was already very good.

5 CONCLUSIONS

We have extended the spectral-element method for global seismic wave propagation developed in Paper I (Komatitsch & Tromp 2002) to incorporate the effects of 3-D mantle and crustal models, the oceans, rotation and self-gravitation in the context of the Cowling approximation. Therefore, the SEM can now accommodate the full
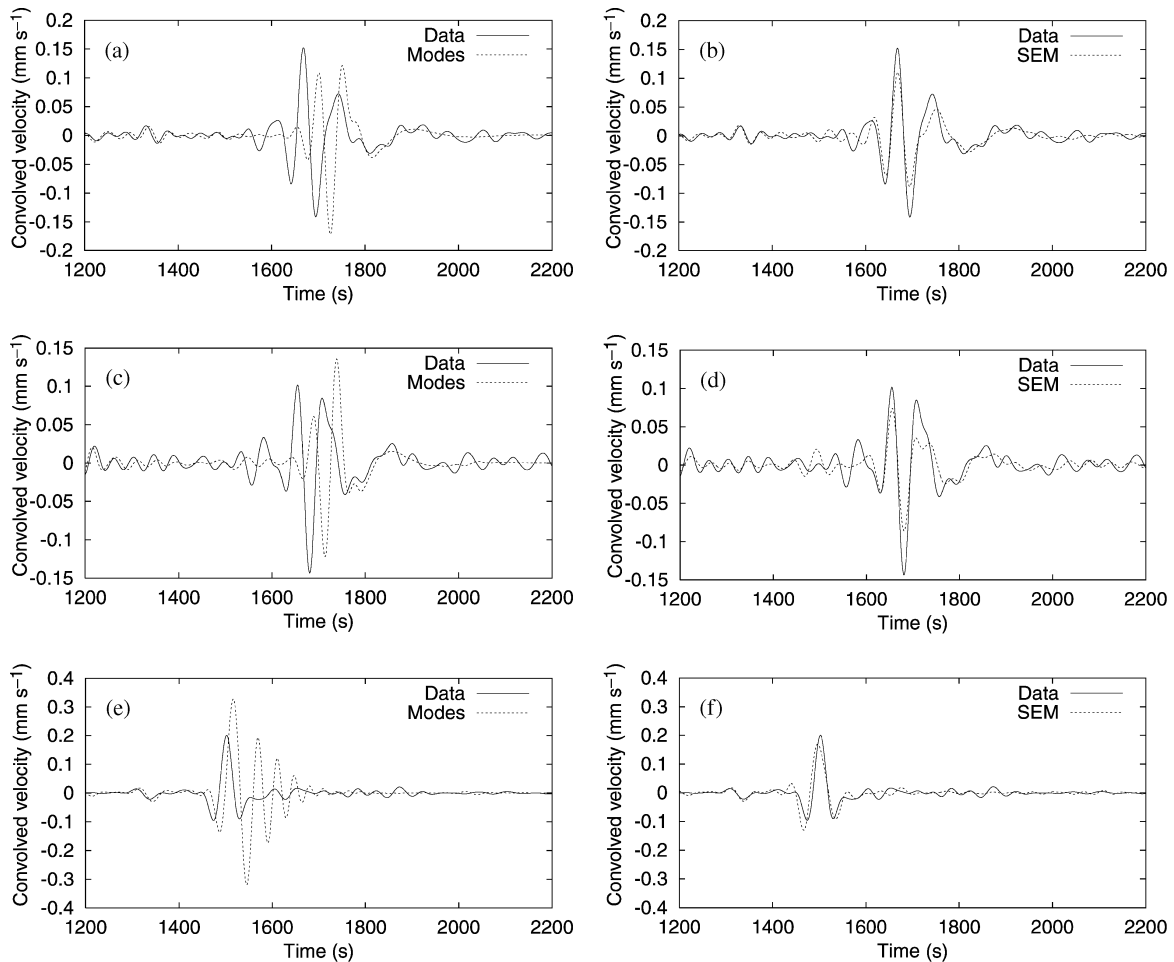
Figure 18. Vertical (top), longitudinal (middle) and transverse (bottom) components of displacement convolved with the instrument response and low-pass filtered at a corner frequency of 40 s at station MAJO in Japan, for the PREM normal-mode solution (left, dotted line) and a fully 3-D SEM simulation (right, dotted line) compared with real data (solid line). The event is located in Vanuatu and the path is therefore mostly oceanic. The epicentral distance is 60°. Note how the PREM normal-mode synthetics predict a Love wave whose duration is much too long, and a Rayleigh wave which arrives much too late. The SEM synthetics incorporate the thin oceanic crust and predict the arrival time of the Rayleigh wave, as well as the short duration of the Love wave.
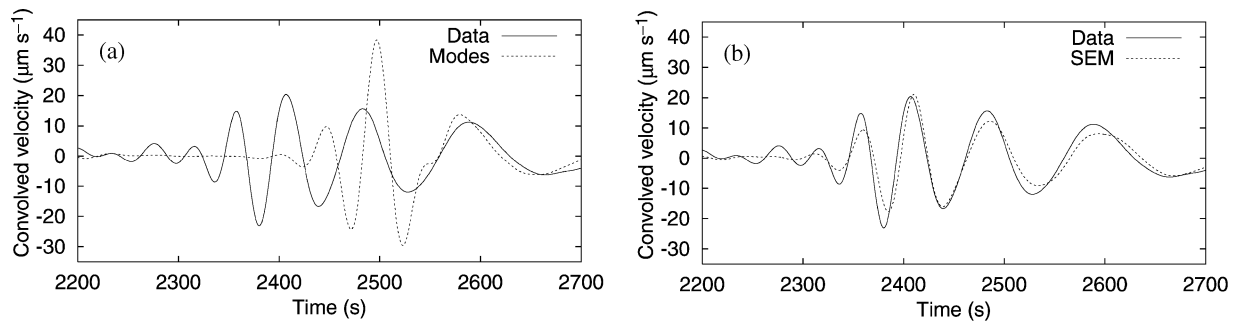
Figure 19. Vertical component of displacement convolved with the instrument response and low-pass filtered at a corner frequency of 40 s at TriNet station PAS in Pasadena, California, for the PREM normal-mode solution (left, dotted line), and a fully 3-D SEM simulation (right, dotted line), compared with real data (solid line). The event is located in Vanuatu and the path is therefore mostly oceanic. The epicentral distance is $86°$. The Rayleigh wave arrives 85 s earlier than in PREM. Note that the 3-D SEM synthetic matches this early arrival very nicely and tracks the phase of the Rayleigh wave quite well.
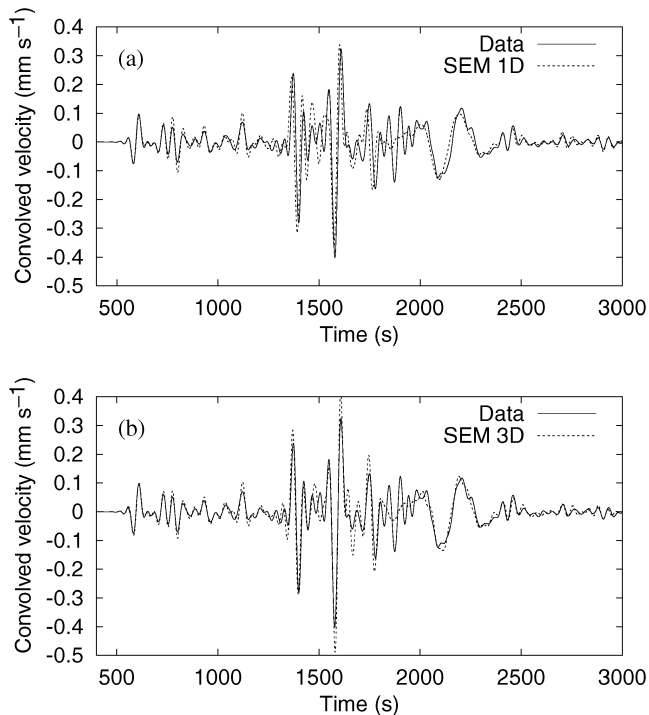
Figure 20. Vertical component of displacement convolved with the instrument response and low-pass filtered at a corner frequency of 40 s at station PAS in Pasadena, California, for an SEM simulation in PREM (top, dotted line) and a fully 3-D SEM simulation (bottom, dotted line) compared with real data (solid line). The event is located in Bolivia and the path is therefore mostly continental. The epicentral distance is $68°$. The 3-D SEM simulation improves the fit to the data significantly, in particular the large *SKS*, *sSKS* and *SS* phases between 1400 and 1700 s, as well as the Rayleigh wave around 2000 s. The improvement is less spectacular than in Figs 18 and 19 because the fit obtained based upon PREM was already very good for this station.

complexity of realistic 3-D Earth models. Specifically, we incorporate lateral variations in *P*-, *S*-wave velocity and density in the mantle, as well as a 3-D crustal model, and we show how to introduce the ellipticity, topography and bathymetry of the Earth. We also show how to take into account the oceans, rotation and self-gravitation. The effect of the oceans on global wave propagation is efficiently introduced based upon an equivalent surface load integral that does not require an explicit meshing of the oceans, thus greatly simplifying the method and reducing the CPU time. We validate the implementations of self-gravitation and the oceans based upon

comparisons with PREM normal-mode synthetics at periods greater than 20 s for self-gravitation and 25 s for the oceans. For long-period multiorbit surface waves we accurately reproduce the effect of self-gravitation up to R_4. Contrary to what is often assumed, we show that for some source–receiver configurations the effects of the oceans, self-gravitation and rotation can be significant. Both self-gravitation and the oceans have the effect of slowing down the Rayleigh wave.

As a first fully 3-D application we consider data from two earthquakes: a shallow 1997 $M_w = 7.4$ event in Vanuatu and the great 1994 $M_w = 8.2$ deep Bolivia event. For the Vanuatu event we show that Rayleigh waves on trans-Pacific paths can arrive more than 85 s earlier than in PREM, and that Love waves are much shorter in duration than in PREM. For the Bolivia event we demonstrate that with a fully 3-D simulation the fit to the data is improved compared with the same calculation in PREM.

We believe that the SEM is the method of choice for the simulation of global seismic wave propagation in fully 3-D Earth models. Thus far, no other technique is capable of accurately incorporating all the complexities associated with this problem. The main current drawback of the SEM lies in the computational cost of the large-scale 3-D simulations. The calculations presented in this paper require 151 processors on a parallel computer, several tens of Gigabytes of distributed memory, and use tens of hours of CPU time, depending on the desired length of the time-series. Such requirements may seem prohibitive, but several factors play in favour of the SEM. First, very efficient and relatively cheap parallel computers such as PC clusters (also known as 'Beowulfs') are now available to individual researchers (Sterling *et al.* 1999; Komatitsch & Tromp 2001). On such machines the SEM offers superior accuracy compared with other techniques, such as finite-difference or pseudospectral methods, for a comparable or even lower cost. Secondly, extremely powerful computers are now under development that will revolutionize parallel computing over the next few years. The world's fastest computer as of 2002, the Earth Simulator at JAMSTEC, has a capacity of 40 Tera floating point operations per second (1 Teraflops = 10^{12} flops). On such a computer we estimate that all the calculations presented in this paper would run in 30 min or less. Fig. 21, adapted from Thomas Sterling's Supercomputing 2000 presentation (Sterling 2000), shows an extrapolation from 1993 to 2010 of the speed of the fastest computer in the world, based upon the Top500 list of supercomputers (Meuer *et al.* 2001). The curve shows that we may reach a computer capable of 1 Petaflop = 1 million Gigaflops = 10^{15} flops around the year 2010. On such a machine the calculations presented in this paper would very likely run in less than 30 s. Fig. 21 also shows a tentative estimate of the expected evolution of processor technology over the next ten years. One can
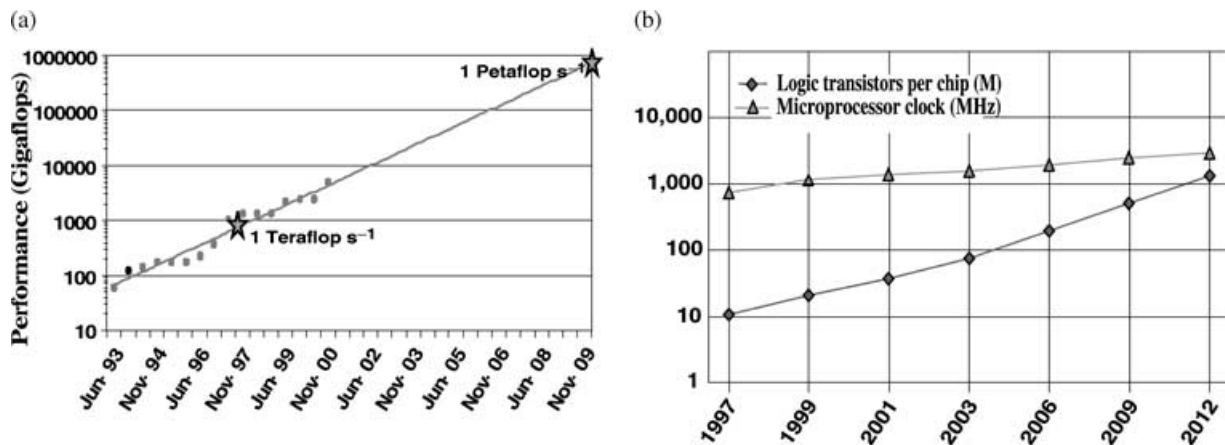
Figure 21. Left: extrapolation from 1993 up to 2010 of the speed of the fastest computer in the world, taken from the Top500 list of supercomputers (Meuer *et al.* 2001). The curve shows that we might reach a computer capable of 1 Petaflop = 1 million Gigaflops = 10^{15} flops around the year 2010. Note that performance has increased by a factor of 100 between 1993 and 2000, and there is reason to believe that it will increase by another factor of 100 over the next decade. Right: projected evolution up to 2012 of the number of logic transistors per microprocessor chip (in millions) and typical microprocessor clock frequency (in MHz). This curve confirms that the number of transistors per processor is going to increase dramatically, which will also play in favour of the possibility of reaching 1 Petaflop computers around the year 2010. Note that, contrary to popular belief, processor clock frequency is not expected to increase far beyond the values currently available ($\simeq$2 GHz). Adapted from Sterling (2000), courtesy Thomas Sterling, CACR, Caltech.

see that microprocessor clock frequency, which is closely related to processor speed, is not expected to increase by a factor of more than 2 or 3, because of technological barriers such as the silicon etching resolution and thermal dissipation. However, the density of integration of logic transistors per microprocessor chip is expected to increase dramatically over the next ten years, another factor that will play in favour of reaching 1 Petaflop computers around 2010 (Sterling & Messina 1995; Sterling 2000).

Considering these technological developments, we are convinced that in the near future the SEM will be routinely used for calculations that take into account the full 3-D complexity of the Earth. For example, one can already imagine centroid-moment tensor (CMT) inversions in fully 3-D Earth models, since the number of unknowns in the inversion is only of order ten. These fully 3-D CMT inversions should reduce the earthquake magnitude threshold in global catalogues considerably, and result in better constraints on location, half-duration and mechanism. In the more distant future, we believe that the SEM will open the door to full-waveform inversions. This will require ∼10 000 forward simulations for hundreds of earthquakes. On Petaflop parallel machines this will become feasible.

REFERENCES

Bassin, C., Laske, G. & Masters, G., 2000. The current limits of resolution for surface wave tomography in North America, *EOS,* **81,** F897, also available at mahi.ucsd.edu/Gabi/crust2.html.

Bernardi, C., Debit, N. & Maday, Y., 1990. Coupling finite element and spectral methods: first results, *Math. Comput.,* **54,** 21–39.

Bernardi, C., Maday, Y. & Patera, A.T., 1994. A new nonconforming approach to domain decomposition: the Mortar element method, in *Nonlinear Partial Differential Equations and Their Applications,* eds Brezis, H. & Lions, J.L., Séminaires du Collège de France, Paris.

Canuto, C., Hussaini, M.Y., Quarteroni, A. & Zang, T.A., 1988. *Spectral Methods in Fluid Dynamics,* Springer-Verlag, New York.

Capdeville, Y., Chaljub, E., Vilotte, J.P. & Montagner, J.P., 2002. Coupling the spectral element method with a modal solution for elastic wave propagation in global Earth models, *Geophys. J. Int.,* submitted.

Chaljub, E., 2000. Modélisation numérique de la propagation d'ondes sismiques en géométrie sphérique: application à la sismologie globale (Numerical modeling of the propagation of seismic waves in spherical geometry: applications to global seismology), *PhD thesis,* Université Paris VII Denis Diderot, Paris, France.

Chaljub, E., Capdeville, Y. & Vilotte, J.P., 2002. Solving elastodynamics in a fluid solid heterogeneous sphere: a parallel spectral element approximation on non-conforming grids, *J. Comput. Phys.,* submitted.

Cowling, T.G., 1941. The non-radial oscillations of polytropic stars, *Mon. Not. R. astr. Soc.,* **101,** 369–373.

Dahlen, F.A. & Tromp, J., 1998. *Theoretical Global Seismology,* Princeton University Press, Princeton.

Dziewonski, A.M. & Anderson, D.L., 1981. Preliminary reference Earth model, *Phys. Earth planet. Inter.,* **25,** 297–356.

Felippa, C.A. & Deruntz, J.A., 1984. Finite-element analysis of shock-induced hull cavitation, *Comput. Methods Appl. Mech. Engrg.,* **44,** 297–337.

Hughes, T.J.R., 1987. *The Finite Element Method, Linear Static and Dynamic Finite Element Analysis,* Prentice-Hall, Englewood Cliffs, NJ.

Komatitsch, D. & Tromp, J., 2001. Modeling of seismic wave propagation at the scale of the Earth on a large Beowulf, *Proc. of the ACM/IEEE*

Supercomputing SC'2001 Conference, published on CD-ROM and on www.sc2001.org.

Komatitsch, D. & Tromp, J., 2002. Spectral-element simulations of global seismic wave propagation—I. Validation, *Geophys. J. Int.,* **149,** 390–412.

Kopriva, D.A., 1996. A conservative staggered-grid Chebyshev multidomain method for compressible flows: part II, a semi-structured method, *J. Comput. Phys.,* **128,** 475–488.

Meuer, H.W., Strohmaier, E., Dongarra, J.J. & Simon, H.D., 2001. Top500 list of supercomputer sites, Tech. rep., University of Mannheim, Mannheim, Germany, available online at http://www.top500.org.

Mooney, W., Laske, G. & Masters, G., 1998. Crust 5.1: a global crustal model at 5 × 5 degrees, *J. geophys. Res.,* **103,** 727–747.

NOAA, 1988. National Oceanic and Atmospheric Administration (NOAA) product information catalog—ETOPO5 Earth Topography 5-minute digital model, *Technical report,* US Department of Commerce, Washington, DC, p. 171.

Park, K.C. & Felippa, C.A., 1980. Partitioned transient analysis procedures for coupled field problems: accuracy analysis, *J. appl. Mech.,* **47,** 916–926.

Ritsema, J., Van Heijst, H.J. & Woodhouse, J.H., 1999. Complex shear velocity structure imaged beneath Africa and Iceland, *Science,* **286,** 1925–1928.

Ronchi, C., Ianoco, R. & Paolucci, P.S., 1996. The 'Cubed Sphere': a new method for the solution of partial differential equations in spherical geometry, *J. Comput. Phys.,* **124,** 93–114.

Rønquist, E.M., 1996. Convection treatment using spectral elements of different order, *Int. J. Num. Meth. Fluids,* **22,** 241–264.

Sadourny, R., 1972. Conservative finite-difference approximations of the primitive equations on quasi-uniform spherical grids, *Mon. Weather Rev.,* **100,** 136–144.

Sterling, T.L., 2000. Petaflops computing: looking back at the future, Tech. rep., California Institute of Technology, Pasadena, California, presented at the Supercomputing 2000 conference, Dallas, Texas, Nov. 2000.

Sterling, T.L. & Messina, P.C., 1995. *Enabling Technologies for Petaflops Computing,* MIT Press, Cambridge.

Sterling, T.L., Salmon, J., Becker, D.J. & Savarese, D.F., 1999. *How to Build a Beowulf, a Guide to the Implementation and Application of PC Clusters,* MIT Press, Cambridge.

Taylor, M., Tribbia, J. & Iskandarani, M., 1997. The spectral element method for the shallow water equation on the sphere, *J. Comput. Phys.,* **130,** 92–108.

Valette, B., 1986. About the influence of prestress upon the adiabatic perturbations of the Earth, *Geophys. J. R. astr. Soc.,* **85,** 179–208.

Valette, B., 1987. Spectre des oscillations libres de la Terre: aspects mathématiques et géophysiques (spectrum of the free oscillations of the Earth: mathematical and geophysical aspects), *PhD thesis,* Université Paris VI Jussieu, Paris.